AVIRIS Calibration and Application in Coastal Oceanic Environments

Kendall L. Carder, Phillip Reinersman, Robert F. Chen, and Frank Muller-Karger

Marine Science Department, University of South Florida, St. Petersburg

Curtiss O. Davis and Michael Hamilton

Jet Propulsion Laboratory

T*he Airborne Visible-Infrared Imaging Spectrometer (AVIRIS) is a test-bed for future spacecraft sensors such as the High-Resolution Imaging Spectrometer and the Moderate-Resolution Imaging Spectrometers planned for the Earth Observing System. To use this sensor for ocean applications, S / N was increased by spatial averaging of images. Post-flight recalibration was accomplished by measuring in situ the water-leaving radiance at flight time, modeling its transmission to the aircraft, and adding modeled atmospheric radiance to that value. The preflight calibration curve was then adjusted until aircraft and modeled total radiance values matched. Water-leaving radiance values from the recalibrated AVIRIS imagery were consistent with in situ data supporting the validity of the approach. Imagery of the absorption coefficient at 415 nm and backscattering coefficient at 671 nm were used to depict the dissolved and particulate constituents of the Tampa Bay plume during late, ebb-tidal conditions.*

INTRODUCTION

The Airborne Visible-Infrared Imaging Spectrometer (AVIRIS) (Vane et al., 1993) of NASA's Jet Propulsion Laboratory is a test-bed for future spacecraft imaging spectrometers such as the High-Resolution Imaging Spectrometer and the Moderate-Resolution Imaging Spectrometer-T instruments planned for the Earth Observing System. AVIRIS was designed largely for high spectral and spatial resolution land applications with target reflectances of 20–50%, whereas water reflectances are typically less than 5%. It has 224 spectral channels from 400 nm to 2400 nm, 20 m square pixels when viewing from 65,000 ft altitude, and about 10–20% of the signal-to-noise (S / N) of the Coastal Zone Color Scanner (CZCS). If the AVIRIS is to produce data of interest to oceanographers, the S / N must be increased 10–20-fold (Hamilton et al., 1991). This increase may be achieved by standard image processing techniques such as spatial averaging and low-pass filtering. For instance, uniform spatial averaging of an $N \times N$ pixel area will yield a nominal N-fold increase in S / N if the noise is incoherent or has a wavelength shorter than N pixels. This increase in S / N is gained at the expense of resolution since the effective pixel size is equal to the size of the area being averaged.

The AVIRIS preflight calibration must be verified or adjusted to be consistent with the in-flight performance of the instrument. The recalibrated data representing total radiance at the sensor may then be partitioned into atmospheric radiance and water-leaving radiance. Comparison of field measurements of water-leaving radiance with values derived from AVIRIS provides the fundamental validation for the recalibration approach to be outlined here.

Finally, application of a predictor-corrector, remote-sensing reflectance model (e.g., Carder and Steward, 1985) provides a measure of the utility of high resolution data for studies of coastal environments.

METHODS

AVIRIS data were collected from a NASA ER-2 aircraft flying at 65,000 ft altitude on two SW–NE flight lines. These lines were flown at about 15:15 Eastern Standard Time on 4 March 1990 and extended from the west Florida shelf into the mouth of Tampa Bay (see Fig. 1). A total of 16 scenes were collected along a shelf transect covered the same day by the R/V *BELLOWS* of the Florida Institute of Oceanography (see Fig. 1a). The shoreward scenes included complex bathymetric and topographic features (see Fig. 1b) that were expected to have effects on the wind and light fields as well as the hydrodynamics.

Ship-Based Data

Chlorophyll a, phenophytin a, remote-sensing reflectance (R_{rs}), above-water downwelling irradiance $[E_d(0^+)]$, subsurface downwelling irradiance $[E_d(z)]$, and subsurface upwelling irradiance $[E_u(z)]$, and radiance $[L_u(z)]$ data were gathered at three stations along the transect between 09:30 h and 13:30 h. Chlorophyll fluorescence was measured continuously between stations. The pigments were determined using the fluorometric method of Holm-Hansen and Riemann (1978) for samples collected with Niskin bottles and filtered onto 25 mm Whatman GF/F glass-fiber filter pads. Particle absorption coefficients (a_p) were determined for separate GF/F pads using the method of Mitchell (1990). The absorption coefficient due to colored dissolved organic matter or gelbstoff (a_g) was determined by the method of Bricaud et al. (1981)

for material passing through preflushed, 47 mm, Nuclepore pads with 0.2-μm pore diameters.

Remote-sensing reflectance measurements were determined using the methodology described in Carder and Steward (1985) and Peacock et al. (1990). To improve spectral resolution to 6 nm, a 200-μm entrance slit was added to the Spectron Engineering radiometer Model 590, and a vertical polarizer was placed in front of the slit to minimize uncertainty about the Fresnel-reflected skylight received in the upwelling radiance path. A 10% gray, diffuse reflector, Spectralon, a NBS-traceable standard from Labsphere, was used to convert downwelling global irradiance to upwelling radiance for measurement by the Spectron radiometer.

A Licor Model 1800 downwelling spectral irradiance meter (Gregg and Carder, 1990) on an adjacent island provided a continuous global irradiance record for this cloud-free day. In-water upwelling radiance and upwelling and downwelling irradiance measurements were collected using a Biospherical Instruments MER–1048 for confirmation of the Spectron water-leaving radiance data. This is an updated version of a Bio-optical Profiling System (BOPS, Smith and Baker, 1984; 1986).

AVIRIS Data

AVIRIS data were provided on 6250 bpi tapes by the AVIRIS Project at the Jet Propulsion Laboratory (JPL). The original 224 spectral channels of data were edited to the 62 channels (400–1000 nm) in the visible and near-infrared useful to ocean remote sensing. Calibration and vignetting-correction files were also provided. After calibration and vignetting corrections were made, the data for each scene formed a data cube consisting of 512 rows by 614 columns by 62 colors. These scenes were manipulated using a combination of Fortran 77 code and Precision Visuals Wave software on a Digital Equipment DEC Station 5000.

Recalibration and Atmospheric Correction

The recalibration process consisted of comparing modeled, upwelling radiance at the aircraft altitude to AVIRIS data for an offshore scene where the chlorophyll concentration was low (0.4 mg/
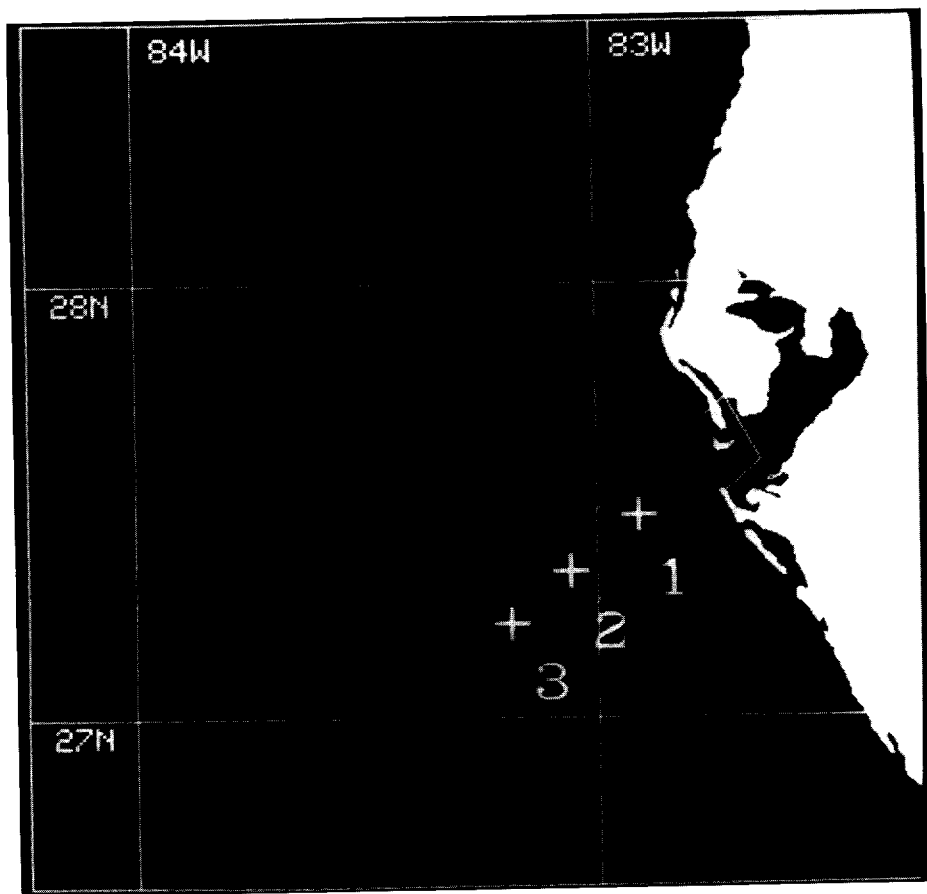
(a)
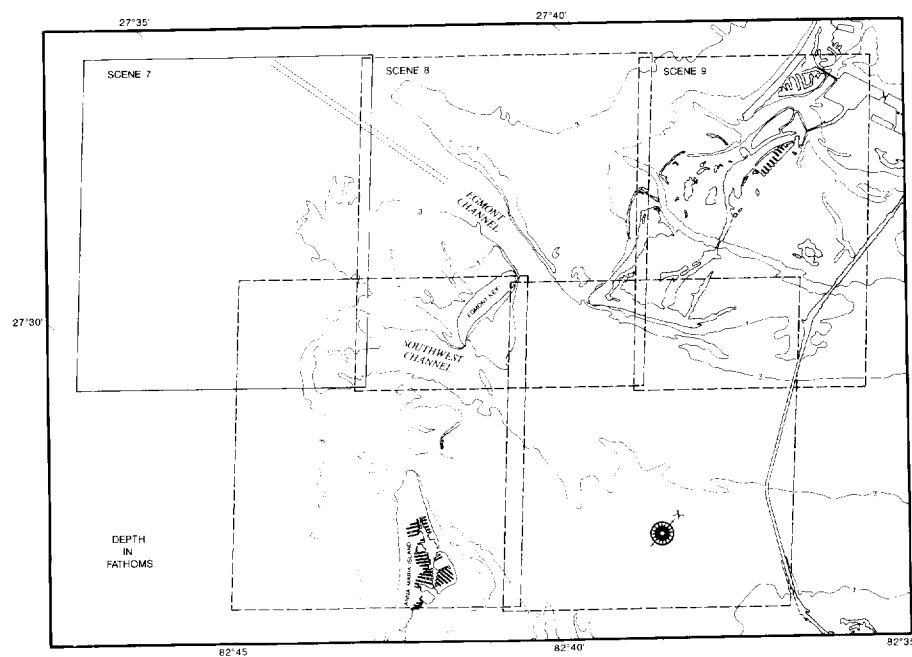
(b)

Figure 1. a) Region covered, imaged by AVIRIS scenes from two flight lines into the mouth of Tampa Bay. Also shown are three calibration stations. b) Detailed schematic of Scene 7 of the north flight line.

m³) and relatively uniform. The modeled data were generated by simulating the atmospheric attenuation of water-leaving radiance (L_w) measured at the scene from the R/V Bellows, and then simulating and adding the other path radiance contributions which would be detected by the AVIRIS radiometer.

The diffuse transmissivity (t_d) of the calibration scene from the surface to altitude was calculated using Lowtran 7 multiple-scattering code. Input parameters for the Lowtran code corresponded to an atmosphere containing a marine aerosol with a boundary-layer, horizontal-path visibility of 60 km. These conditions were characteristic of the atmosphere at Station 3 at the time of the overflight, and were assumed constant along the flight line. The relative positions of the sun, the aircraft, and the observed scene were also necessary inputs for the Lowtran 7 simulations. With these data the Lowtran 7 model was also able to produce simulations of the atmospheric path radiance, $L_p(\theta_-, \lambda)$, skylight that is specularly reflected by the sea surface and diffusely transmitted to the AVIRIS instrument, $\rho(\theta)t_d(\theta, \lambda)L_{pr}$ (θ_+, λ), and path radiance scattered from specularly reflected, diffusely transmitted solar irradiance, $\rho(\theta_\odot)t_d(\theta_\odot, \lambda)L_{pr}(\theta_+, \lambda)$, which were also detected by the AVIRIS. These contributions were summed to provide the simulated total radiance, $L_t(\theta_-, \lambda)$, available at AVIRIS:

$$L_t(\theta, \lambda) = L_{pr}(\theta_+, \lambda)[\rho(\theta)t_d(\theta, \lambda) + \rho(\theta_\odot)t_d(\theta_\odot, \lambda)]$$
$$+ t_d(\theta, \lambda)L_w(\theta, \lambda) + L_p(\theta_-, \lambda). \qquad (1)$$

Here $\rho(\theta)$ and $\rho(\theta_\odot)$ are the Fresnel reflectance values of the sea surface for reflected skylight and sunlight, where $\theta_\odot$ and θ are the solar and pixel-sensor zenith angles, respectively. $\theta_{+/-}$ are the forward and backward scattering angles involved in viewing reflected skylight and direct path radiance, respectively. Note that the observation geometry must be chosen to avoid direct sun glint into the sensor.

The reflected downwelling path radiance reaching AVIRIS was determined by applying Lowtran 7 as if the sensor were on the ocean, viewing space in the direction of the AVIRIS instrument. This radiance was subsequently reduced by specular reflectance and diffuse transmittance to simulate the radiance contribution at AVIRIS. The upwelling skylight scattered from specularly reflected sunlight is also due to forward

scattering. It is similar to reflected skylight reaching AVIRIS except that it has been reduced by diffuse transmittance of the downwelling solar irradiance and by its specular reflectance prior to being scattered as path radiance to AVIRIS.

The total radiance measured by AVIRIS, L_{tm}(Sta. 3), at Station 3 was adjusted to correspond to the radiance calculated, L_{tc}(Sta. 3), at Station 3 by multiplying by a calibration adjustment factor CAL. At all other stations AVIRIS radiance values $L_{tm}(\lambda)$ were multiplied by CAL, where

$$CAL(\lambda) = L_{tc}(\text{Sta. } 3, \lambda) / L_{tm}(\text{Sta. } 3, \lambda). \qquad (2)$$

Figure 2 compares spectral values of CAL(λ), labeled USF, with the preflight calibration curve, labeled JPL. Note that the major difference between the curves occurred at short wavelengths where both the solar irradiance illuminating the scene and the responsivity of silicon detectors are low relative to those at longer wavelengths. Vibrational and thermal effects are thought to be the major reasons for changes between laboratory calibration curves of AVIRIS and those required to match field measurement, although the effects of errors in Lowtran 7 parameterization are also included in the calibration procedure. The Lowtran 7 errors are systematic in nature, and should have little effect on the retrieved $L_w(\lambda)$ values for scenes processed using the same Lowtran 7 parameters and algorithm for removal of atmospheric effects.

The water-leaving radiance for each pixel in each scene was calculated by solving Eq. (1) for $L_w(\lambda)$, using $L_{tm}(\lambda)*CAL(\lambda)$ for $L_t(\lambda)$. Lowtran 7

Figure 2. Original (JPL) and adjusted (USF) calibration curves for AVIRIS.
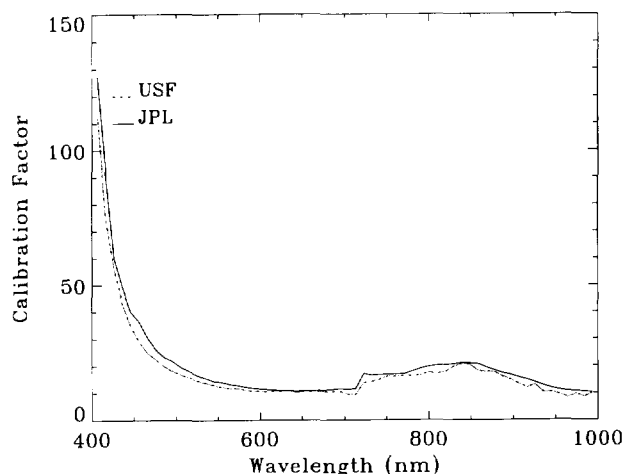
parameters determined at Station 3 for the atmosphere were used along the entire flight line to provide the atmospheric correction terms. The water-leaving radiance values determined for wavelengths greater than 800 nm were examined to ensure that these values did not differ significantly from zero. Had nonzero values occurred, they would have suggested that a change in visibility or aerosol optical thickness had occurred, since with water molecular absorption coefficients greater than 2.4 m^{-1} for these wavelengths (Smith and Baker, 1981), negligible radiance leaves the water except under unusually turbid conditions.
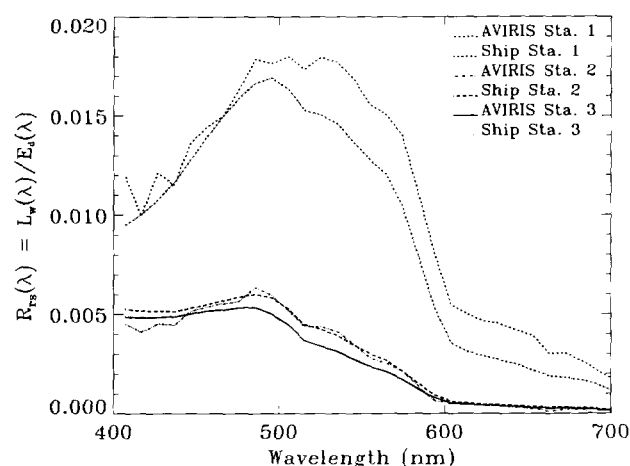
The vicarious calibration of AVIRIS was performed using an average of 100 × 100 pixels of data from the offshore scene of the north flight line and coincident *in situ* data from Station 3. The AVIRIS data were then corrected for atmospheric effects as described above and normalized with downwelling global irradiance calculations using Lowtran 7 code to form remote-sensing reflectance $R_{rs}(\lambda)$ curves.

The best fit resulted using a specified Lowtran visibility of 60 km for a marine type aerosol with a wind speed of 6–8 m / s. The ER-2 aircraft was distinctly visible from the ground, corroborating model-derived high visibility.

RESULTS

Figure 3 compares remote-sensing reflectance curves derived from AVIRIS data with those of

Figure 3. Comparison of $R_{rs}(\lambda)$ spectra from AVIRIS and *in situ* data.

field data. A perfect match occurs at the calibration station (Sta. 3) as required by the vicarious calibration method. Tidal currents near Tampa Bay and a 3–5 h delay between field measurements and the AVIRIS overflight rendered curves for Stations 1 and 2 less comparable. Modeling can be used to characterize the differences between the field and AVIRIS-derived curves for Station 2, however.

For an optically thick, homogeneous ocean (e.g., well-mixed, deep water), the following equation (Morel and Prieur, 1977; Carder and Steward, 1985) can be applied:

$$R_{rs}(\lambda) = L_w(\lambda) / E_d(\lambda)$$
$$= \{0.33 b_b(\lambda) / [a(\lambda) + b_b(\lambda)]\}(t / n)^2 / Q, \quad (3)$$

where Q is $E_u(\lambda) / L_u(\lambda)$, only weakly dependent upon λ (Gordon and Morel (1983), $b_b(\lambda)$ is the backscattering coefficient of water and its suspended particles, and the squared term provides for the radiance divergence and sea–air transmitance, t, of radiance leaving the water. The index of refraction of seawater, n, is about 1.334. This equation contains no provision for transpectral phenomena such as water-Raman scattering (considered negligible for near-shore environments) or fluorescence due to colored, dissolved organic matter (CDOM) and chlorophyll a (not necessarily negligible for certain wavelengths). Provision for these can be made by adding an additional term (e.g., see Gordon, 1979; Carder and Steward, 1985; Stavn, 1990; Marshall and Smith, 1990).

For an optically shallow environment (e.g., depths shallower than about 2.0 optical thicknesses), bottom reflectance needs to be considered. Equation (3) can be modified as follows:

$$R_{rs}(\lambda)_s = R_{rs}(\lambda)_d(1 - \exp\{-[k_d(\lambda) + k_u(\lambda)]D\})$$
$$+ (t / n)^2(a / \pi)\exp\{-[k_d(\lambda) + k_u(\lambda)]D\}, \quad (4)$$

where the subscripts s and d depict shallow- and deep-water conditions, a is the bottom albedo, the bottom reflectance is considered to be Lambertian [e.g., $E_u(\lambda) = \pi L_u(\lambda)$ at the bottom], and D is the water-column depth. The term $(1 - \exp\{-[k_d(\lambda) + k_u(\lambda)]D)$ only becomes important when the depth D is smaller than about 0.5 optical depths. The diffuse attenuation coefficients k_u and k_d are for upwelling and downwelling light, respectively, and are largely a function of $a(\lambda) + b_b(\lambda)$ multiplied by the average slant-path enhancement of the rays (see Kirk, 1983) relative to the vertical.
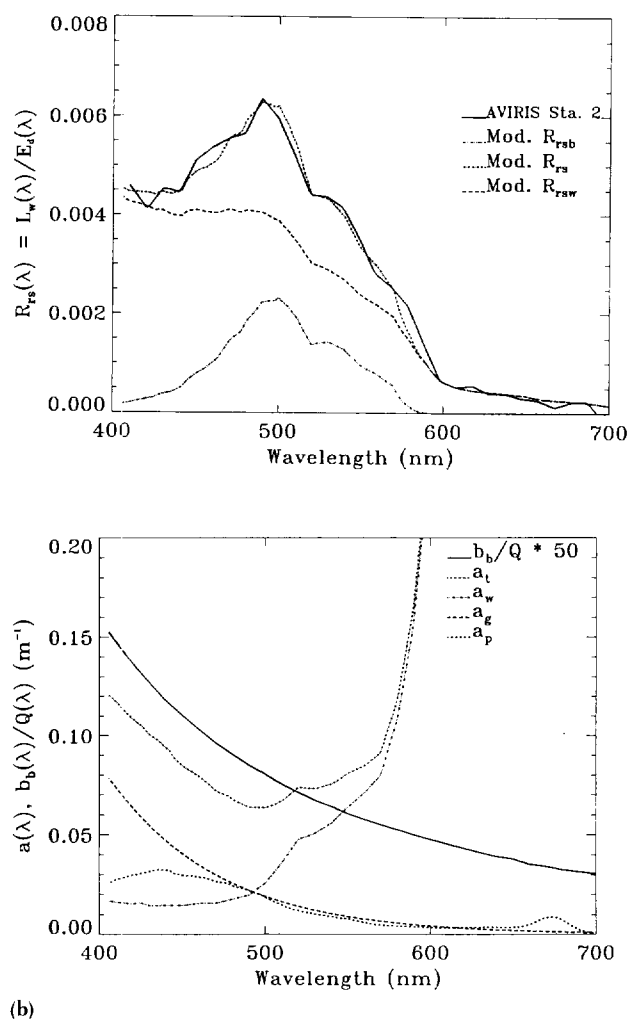
(b)

Figure 4. a) $R_{rs}(\lambda)$ spectra from AVIRIS and a model for Station 2. The contributions attributed to bottom reflection (MOD. R_{rsb}) and water-column reflectance (MOD. R_{rsw}) are shown separately. b) Absorption and backscattering coefficients measured at Station 2 and used to derive the model results in Figure 4a.

Figure 4a provides an example of the utility of high-spectral-resolution AVIRIS data for model applications. It compares a model-derived, remote-sensing reflectance curve to the AVIRIS curve for Station 2. The model uses the absorption coefficients and the ratio of the backscattering coefficient to Q shown in Figure 4b, and the bottom-reflected curve of Figure 4a. This curve was modeled for a 21 m, 0.55 albedo bottom reflection. The absorption values are measurements made at Station 2 adjusted slightly to compensate for changes due to plume movement. The pigment absorption for the AVIRIS model was reduced by 20%, and the CDOM absorption was increased by 15%. The ratio of the backscattering

coefficient to the Q factor remained the same. A subsequent paper (Lee et al., forthcoming) will detail the modeling methodology.

The primary purpose of this modeling example is to demonstrate some of the optical complexity found in even the deeper waters of the west Florida shelf environment. It also helps to demonstrate that high-spectral-resolution data such as AVIRIS provides are critical for quantifying the multiple components that contribute to the water-leaving radiance of coastal environments.

The spectral effect of moving from offshore to nearshore can be seen in the row-averaged, remote-sensing-reflectance spectra of Figure 5. This figure depicts a transition zone from shelf waters (13 m) to a shoal region (6 m) heavily influenced by the ebb, tidal plume leaving Tampa Bay. This region is 4–14 km SW of Egmont Key (Scene 7 in Fig. 1b). Note the gradual shoreward increase in the spectral values until pixel row 400, where a rapid increase is apparent. Suspended sediment, CDOM, particle absorption, and bottom reflection all increase shoreward and gradually confound the spectra.

Interpretations of the data are less complex for deeper waters or when using the longer wavelengths for the shallow waters. With a bottom albedo of 0.5, little or no bottom reflection effect is expected for waters deeper than about two attenuation depths. This applies to waters deeper than about 5 m since red wavelengths (> 670 nm) are absorbed by water molecules at a rate greater than 0.43 m^{-1}. For these waters, one can apply Eq. (3) instead of Eq. (4).

Figure 6 provides a comparison of $R_{rs}(671)$ with $b_b(671)$ for the same row-averaged shoreward transect of Scene 7 as is shown in Figure 5. Note the similarity in shoreward trends along the transect for the two curves except for the most shoreward row numbers. This indicates that even though there is a shoreward growth of $b_b(671)$, it still remains small enough until about row 400 that it does not significantly affect the denominator of Eq. (3), which is dominated by the water absorption coefficient, 0.43 m^{-1}. For green wavelengths with absorption coefficients of about 0.07 m^{-1} or less, backscattering coefficient values of as little as 0.01 m^{-1} become very important to the denominator, and the remote-sensing reflectance curve would rise nonlinearly and much more slowly in progressing shoreward than would the
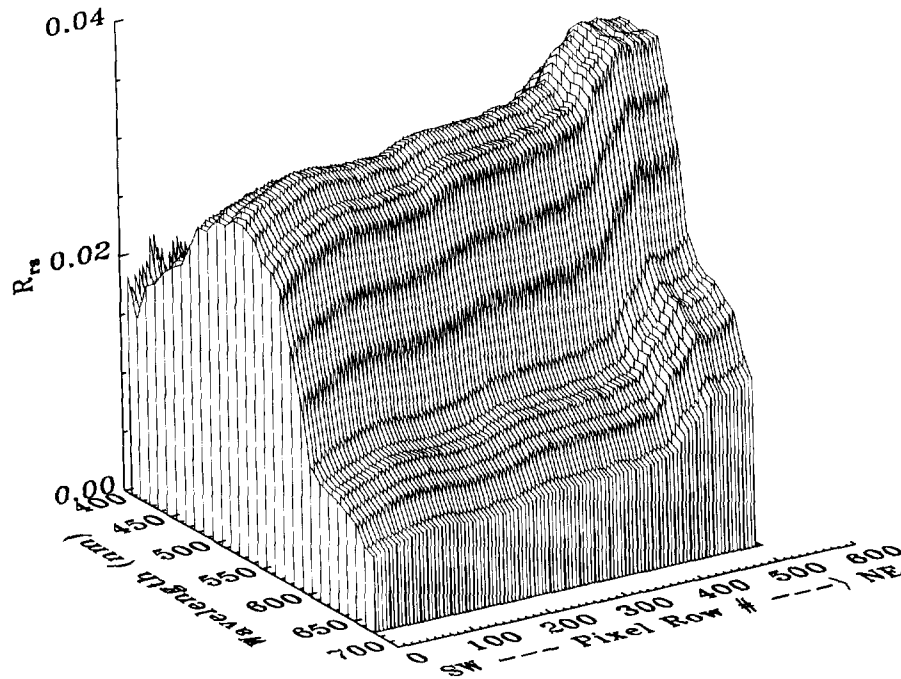
Figure 5. Row-averaged spectra of $R_{rs}(\lambda)$ for Scene 7. Each row is 20 m wide.

curve for the back-scattering coefficient. This example cautions against use of $L_w(\lambda)$ directly or in spectral ratios as a surrogate measure of suspended particulate matter (SPM) in nearshore environments.
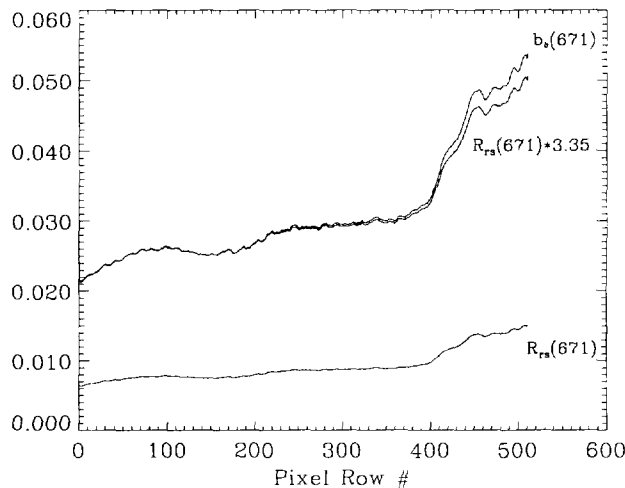
The horizontal variation of the backscattering coefficient is illustrated in Figure 7. In this nearshore environment, the variability in the backscattering coefficient is significantly affected by suspended sediments carried by the ebb tidal currents

Figure 6. Shoreward variation of row-averaged values of $R_{rs}(671)$ and $b_b(671)$ for Scene 7. A curve of $R_{rs}(671*3.35$ is shown juxtaposed with $b_b(671)$ for shape comparisons.
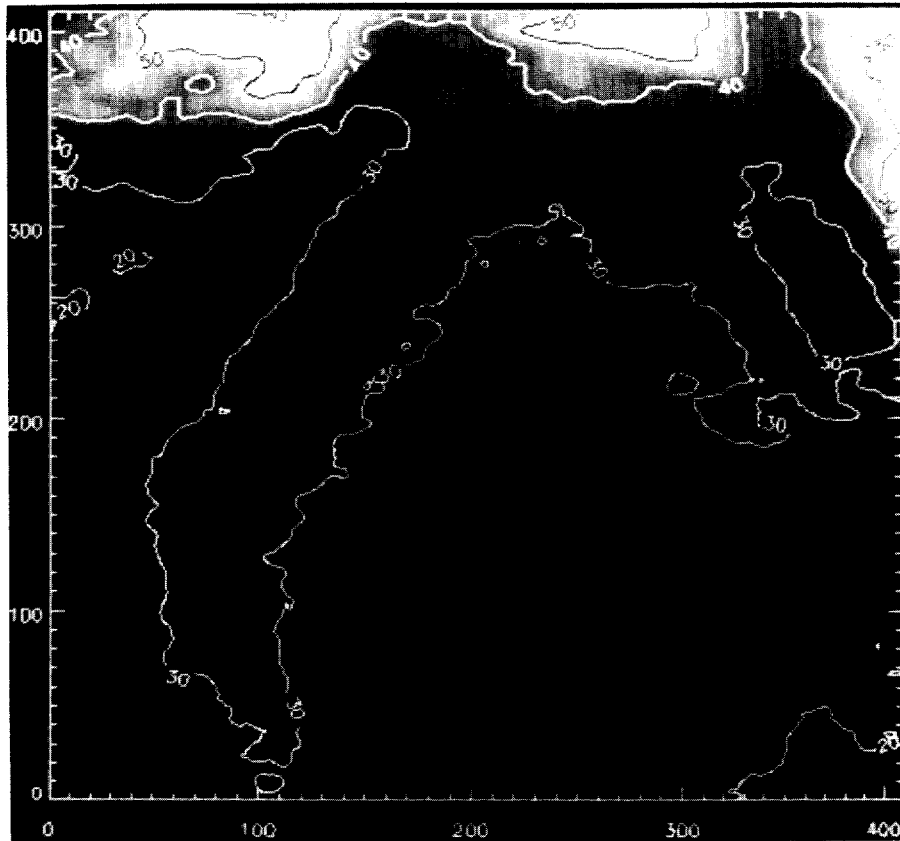

from Tampa Bay and locally resuspended from shoal areas by waves from the northwest. These shoals are located mostly shoreward of Scene 7. The tidal currents usually flow out from channels north and south of Egmont Key (Fig. 1b), and the flows from these two conduits appear to converge at the bright, central shoals in the top-central portion of the scene. The resulting sediment plume dominates the central portion of the image. Beneath this plume water depths increase offshore to 13 m.

A second shoal region is found offshore from Anna Maria Island which is influenced by waters leaving Southwest Passage (the dark region in the upper right-hand portion of the image). Here the diverging current appears to suspend and carry sediment streamers offshore as well. It is not clear from this image how much of the backscattering is due to wave-suspended, sandy sediments that will rapidly settle out of the water column, and how much is due to organic particles and fine sediments which may be transported significant distances. Comparison with a plume image dominated by a more conservative constituent such as CDOM will at least permit the evaluation of plume dilution effects.

The effects of increased CDOM and particle absorption nearshore can perhaps be more easily visualized for the shorter wavelengths by solving

Figure 7. Horizontal variation of $b_b(671)*1000$ for Scene 7. Values have been smoothed by a 14 × 14-pixel boxcar average to increase S / N and to reduce contour complexity. (Note: Rotate 90° clockwise to compare with Figure 1b.)

the deep-water, remote-sensing reflectance equation in terms of the absorption coefficent:

$$a'(\lambda) = b_b(\lambda)[-1 + 0.33 / R_{rs}(\lambda)](t/n)^2 / Q. \quad (5)$$

In shallow water and for the shorter, more transparent wavelengths, perturbations due to bottom reflections and fluorecence may be manifest in the "perturbed" absorption spectra, $a'(\lambda)$. For large, whitish, suspended sediment particles, the backscattering coefficient will be nonspectral, allowing $b_b(\lambda)$ to be determined at 671 nm with the above equation under deep-water conditions by assuming that $a'(671) = 0.43$, the water molecular absorption coefficient. The derived $b_b(671)$ value can then be used in Eq. (5) for all wavelengths.
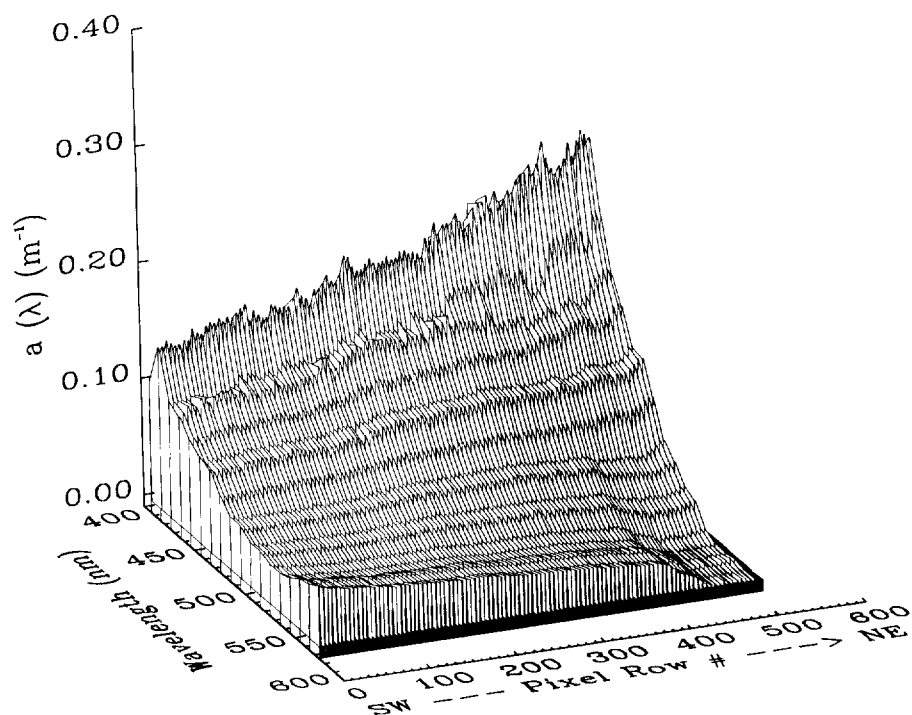
Figure 8 shows the shoreward, row-averaged, perturbed absorption coefficient for Scene 7 from two perspectives. Note that all 671 values are 0.43 m⁻¹, and the $a'(\lambda)$ values centered about 550 nm decrease shoreward to less than zero, while $a'(\lambda)$ values near 400 nm increase shoreward. This dichotomy can be explained by the following observations based upon the model results of Figure 4: 1) The $a'(\lambda)$ values near 400 nm are not seri-

ously affected by bottom reflection, and 2) the values broadly centered about the absorption minimum near 550 nm are affected by bottom reflectance. These effects, which are not specifically treated in Eq. (5), perturb or decrease the actual absorption values since they enhance the $R_{rs}(\lambda)$ values above those provided by the deep-water equation.

The absorption values near 415 nm are large enough that an optical depth of 2.0, $[2*\cos \theta_o / (a + b_b)]$, is typically shallower than the depths in Scene 7. Here, the solar zenith angle was 49.5°. Thus, only the perturbed absorption coefficients near the red and blue ends of the spectrum provided reasonable estimates for the actual or unperturbed absorption values. For the intervening wavelengths, parameters to solve Eq. (5) must be measured and / or inferred from predictor-corrector, multispectral models (e.g., see Fig. 3 results) in order to derive realistic values of the absorption coefficient.

The ebb tidal plume is perhaps best characterized by the absorption coefficient at 415 nm (see Fig. 9). At this short wavelength, the absorption

(a)
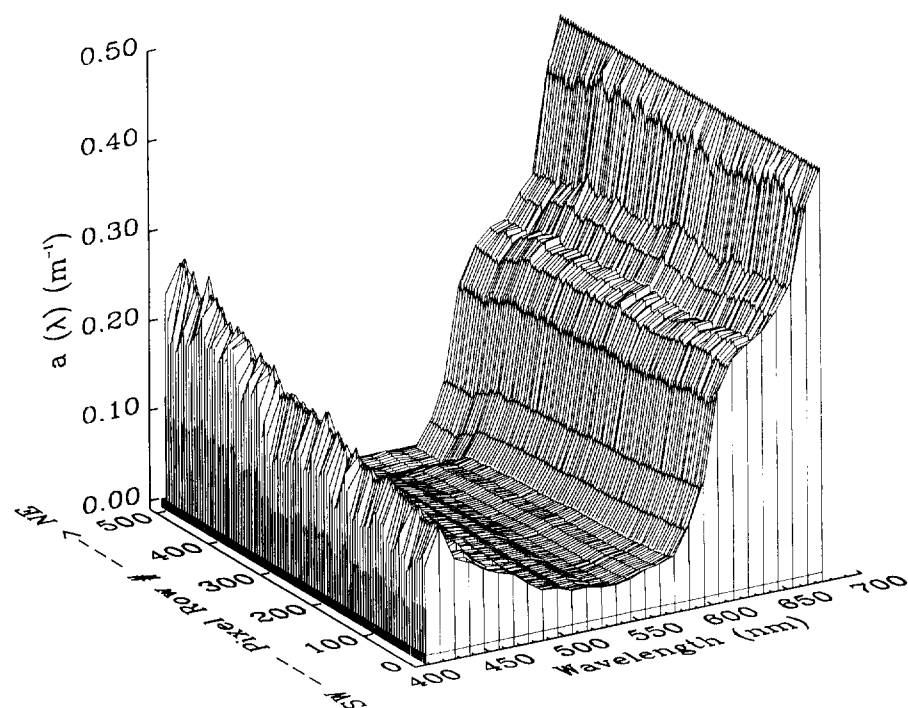
(b)

Figure 8. Shoreward variation in row-averaged spectra of the perturbed absorption coefficient $a'(\lambda)$, shown from two perspectives.

coefficient for nearshore waters can be dominated by CDOM (see Carder et al., 1989; 1991), a refractory, rather conservative constituent. The chlorophyll a concentration just to the west of this scene at Station 1 was 1.2 mg m^{-3}, so phytoplankton probably contributed less than 0.03 m^{-1} to the absorption coefficient at 415 nm.

DISCUSSION

Coastal environments can offer severe challenges to the quantitative interpretation of remotely sensed color data. This is due to the potential mix in residence of dissolved and particulate constituents, their variable absorptive, scattering, and
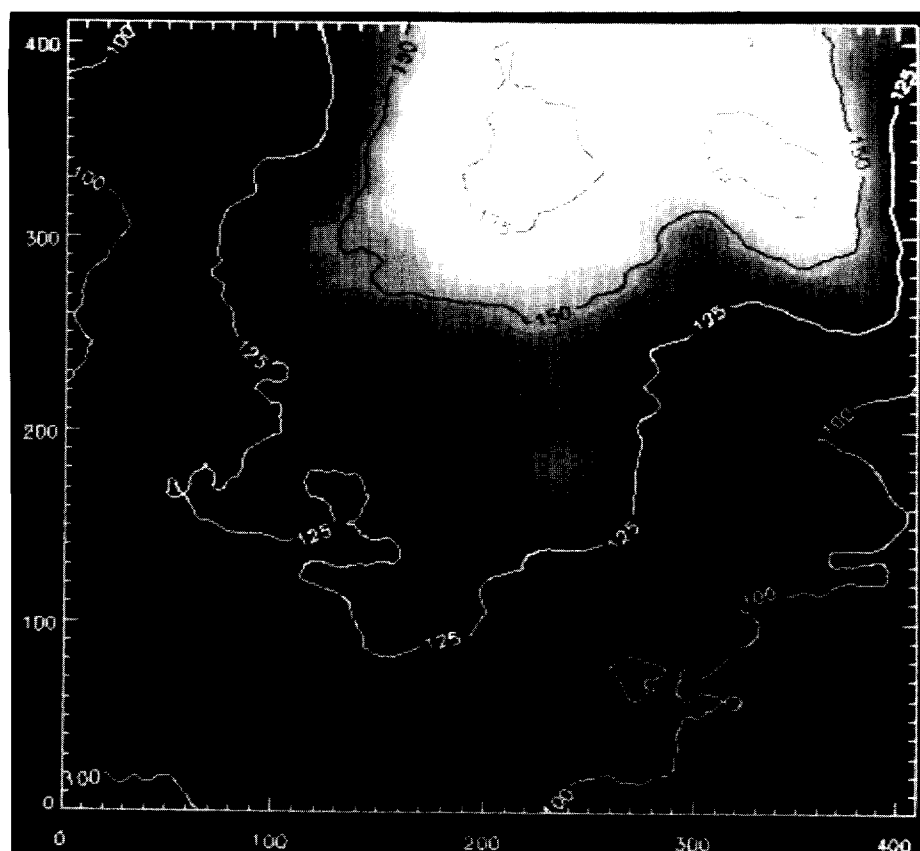
Figure 9. Horizontal variation in the absorption coefficient [$a(415)$]* 1000 for Scene 7. Values have been smoothed by spectrally averaging the three spectral channels centered about 415 nm and applying a 50 × 50-pixel, boxcar average to increase S / N about 85-fold and to reduce contour complexity. (Note: Rotate 90° clockwise to compare with Figure 1b.)

fluorescent optical properties, as well as the reflectance effects of variable bottom depth and albedo.

For waters as deep as 21 m, the bottom-reflected, water-leaving radiance provided as much as 20% of the $R_{rs}(\lambda)$ signal at 490 nm and 15% at 550 nm (see Fig. 4a). For 440 nm and shorter wavelengths, the contributions were progressively smaller than 8%. This trend is expected to increase shoreward and decrease offshore, with the bottom effects adding to the uncertainty of algorithms using spectral data between about 420 nm and 580 nm. For very shallow water (e.g., < 5 m), bottom effects will be apparent over the entire visible spectrum. Thus, chlorophyll a and CDOM algorithms using spectral reflectance ratios such as 443:550 and 410:443, respectively (e.g., see Gordon and Morel, 1983; Carder et al., 1991), will suffer some distortion due to bathymetry even in relatively deep waters (> 25 m) for coastal Florida and similar environments.

AVIRIS data, by means of its continuous, high-resolution spectral coverage, have been found useful as inputs to $R_{rs}(\lambda)$ models capable of parti-

tioning the typical spectral contributors to coastal Florida scenes. Thus, bottom effects can be deconvolved from other spectral contributors, and each can be separately quantified (see Fig. 4).

At wavelengths where the spectra are dominated by a single variable and where bottom effects are small to negligible, the problem is simplified, and individual constituents may be quantified. Thus, for waters deeper than 5 m or 6 m the backscattering coefficient at 671 nm was derived, and varied by a factor of nearly 3 across a scene. Had measurements of suspended particulate matter concentration (SPM) been available, $b_b(671)$ could have been compared to SPM measurements at control sites. Then maps of $b_b(671)$ could have been interpreted in terms of SPM. For such an exercise, multiple ships / boats would be needed, however.

The Tampa Bay plume appears to have flowed out largely through Southwest Passage, to the south of Egmont Key, rather than through Egmont Channel and west out the ship channel, to the north of the key. This unusual outflow pattern may have been induced by the brisk northwest-

erly winds (6–8 m/s), which also contributed to the wave-generated turbulence suspending the shoal sediments (see Fig. 7) north and west of the key.

After leaving Southwest Passage, the plume moved northwestward to reside north of center for the offshore part of the scene. The absorption coefficients ranged from a high in excess of 0.175 m^{-1} near Southwest Passage to an offshore low less than 0.10 m^{-1}, a nearly twofold reduction across the scene due largely to dilution.

The distribution of suspended sediment as indicated by the backscattering coefficient (Fig. 7) varied by a factor of 3 across the scene. Since dilution effects can reduce $b_b(\lambda)$ by less than a factor of 2, about one-third of the decrease can be attributed to sedimentation.

The method developed for deriving $b_b(671)$ can be used for depths as shallow as 1 m if the wavelength is changed to 750 nm. This results from the fact that for this wavelength the water absorption coefficient is 5.74 times as large as it is at 671 nm. Because of the much smaller $R_{rs}(\lambda)$ values expected at 750 nm, however, significant increases are required in the S/N and the precision needed in removing atmospheric effects from the AVIRIS data.

Improvement in S/N cannot be met by averaging more pixels in the near-shore environment, however, because horizontal mixing scales and bottom-roughness scales typically shorten for shallower waters. For short wavelengths, we have already increased S/N by about 85 (see Fig. 9), but this results in an effective resolution element of about 1 km. Nearshore bathymetric features such as ship channels and shoal areas have much finer resolution than 1 km, so such extensive pixel averaging is not suitable for scenes found shoreward of Scene 7.

To quantify optical constituents in the short wavelength region of AVIRIS for environments closer to Tampa Bay, more sensitivity is needed. Also, application of $R_{rs}(\lambda)$ models to separate overlapping spectral components of the radiance field will be practically mandatory. For the more sensitive spectral channels located near 550 nm that would play an important role in imaging bathymetric features (see Fig. 2), the sensitivity is about sixfold that found at 415 nm, and the L_w values are at least a factor of 2 larger. Thus, reasonable S/N values can be expected from AVIRIS even

for box-car-averaged data with an effective resolution of 100 m or less. Nevertheless, unless the horizontal variation of $a(\lambda)$ and $b_b(\lambda)$ are considerably less than was found for Scene 7, separating the bottom effects from the variable attenuation effects will be difficult and will require data from spectral channels with smaller S/N than found near 550 nm.

CONCLUSIONS

The application of AVIRIS data to a study of a coastal environment on the west Florida shelf was accomplished by vicariously calibrating AVIRIS and removing the atmospheric effects from the data. The calibrated sensor provided spectral values of water-leaving radiance that were consistent with values measured from a research vessel and with modeled values, provided that the S/N was increased by averaging data.

The S/N was increased for water-leaving radiance by about 14-fold for red wavelengths and about 50-fold for blue wavelengths. This resulted in an effective spatial resolution of 280 m for the backscattering coefficient at 671 nm, and 1000 m for the absorption coefficient at 415 nm. The decrease in spatial resolution from the single-pixel value of 20 m at nadir is tolerable for offshore environments such as Scene 7 and beyond, where larger horizontal mixing scales are expected. For regions inshore of Scene 7 the natural length scales of channels, shoal areas, keys, and grass flats suggest horizontal gradients in bottom reflectance and water properties that are certainly less than 1000 m, and less than 280 m in many places.

To accurately assess these inshore optical environments, either more signal or less noise is required. Studies that can make use of wavelengths from 500 nm to 570 nm will gain both from higher sensor responsivity and from increased signal than found at 415 nm. The bottom reflectance at these wavelengths will play a major role in the signal, however, so extreme care must be taken to separately account for absorption, backscattering, and bathymetric effects. For this wavelength range, pixel-averaging of as little as 7×7 can be used. To average fewer than this number of pixels is not recommended since a coherent noise equivalent to 7 spatial pixels was

manifest in the AVIRIS data to at least 4 March 1990.

More recent AVIRIS data sets have reduced levels of coherent noise than our data set contained (e.g., see Hamilton et al., 1991), and planned upgrades to AVIRIS may increase signal levels by two- to fourfold at blue wavelengths. Based upon our experience, the increased S/N expected for AVIRIS bodes well for coastal applications requiring an effective spatial resolution of 100–200 m. In the meantime, coastal applications requiring high-spectral resolution can be accomplished with AVIRIS assuming that spatial resolution of better than about 250 m is not required.

REFERENCES

Bricaud, A., Morel A., and Prieur, L. (1981), Absorption by dissolved organic matter in the sea (yellow substance) in the UV and visible domains, *Limnol. Oceanogr.* 26:43–53.

Carder, L. L., and Steward, R. G. (1985), A remote-sensing reflectance model of a red tide dinoflagellate off west Florida, *Limnol. Oceanogr.* 30:286–298.

Carder, K. L., Steward, R. G., Harvey, G. R., and Ortner, P. B. (1989), Marine humic and fulvic acids: Their effects on remote sensing of ocean chlorophyll, *Limnol. Oceanogr.* 34:68–81.

Carder, K. L., Hawes, S. K., Baker, K. A., Smith, R. C., Steward, R. G., and Mitchell, B. G. (1991). Reflectance model for qualifying chlorophyll a in the presence of productivity degradation products. *J. Geophys. Res.* 96, (No. C11):20599–20611.

Gordon, H. R. (1979), Diffuse reflectance of the ocean: The theory of its augmentation by clorophyll a fluorescence at 685 nm, *Appl. Opt.* 18(8):1161–1166.

Gordon, H. R., and Morel, A. (1983), *Remote Assessment of Ocean Color for Interpretation of Satellite Visible Imagery: A Review*, Springer-Verlag, New York.

Gordon, H. R., Clark, D. K., Brown, J. W., Brown, O. B., Evans, R. H., and Broenkow, W. W. (1983), Phytoplank-

ton pigment concentrations in the Middle Atlantic Bight: comparison of ship determinations and CZCS estimates, *Appl. Opt.* 22:20–36.

Gregg, W. W., and Carder, K. L. (1990), A simple 1 nm resolution solar irradiance model for cloudless maritime atmospheres, *Limnol. Oceanogr.* 35:1657–1675.

Hamilton, M., Davis, C. O., Pilorz, S. H., Rhea, W. J., and Carder, K. L. (1991), Examination of chlorophyll distribution in Lake Tahoe, using the Airborne Visible and Infrared Imaging Spectrometer (AVIRIS), in *Proceedings of the Third AVIRIS Workshop*, JPL Publ. 91-28, Pasadena, CA.

Holm-Hansen, O., and Riemann, E. (1978), Chlorophyll-*a* determinations: improvement in methodology, *Oikos* 30: 438–447.

Kirk, J. T. O. (1983), *Light and Photosynthesis in Aquatic Ecosystems*, Cambridge University Press, Cambridge.

Lee, Z., Carder, K. L., Hawes, S. K., Steward, R. G., Peacock, T. G., and Davis, C. O. (forthcoming), An interpretation of high spectral resolution remote sensing reflectance, in *Optics of the Air-Sea Interface: Theory and Measurement*, Leland Estep, ed., Proc. SPIE, 1749.

Marshall, B. R., and Smith, R. C. (1990), Raman scattering and in-water ocean optical properties, *Appl. Opt.* 29:71–84.

Mitchell, B. G. (1990), Algorithms for determining the absorption coefficients for aquatic particulates using the Quantitative Filter Technique, in *Ocean Optics X*, Proc. SPIE 1302, pp. 137–148.

Morel A., and Prieur, L. (1977), Analysis of variations in ocean color, *Limnol. Oceanogr.* 22:709–722.

Peacock, T. P., Carder, K. L., Davis, C. O., and Steward, R. G. (1990), Effects of fluorescence and water Raman scattering on models of remote sensing reflectance, in *Ocean Optics X*, Proc. SPIE 1302, pp. 303–319.

Roesler, C. S., Perry, M. J., and Carder, K. L. (1989), Modeling *in situ* phytoplankton absorption from total absorption spectra in productive inland marine waters, *Limnol. Oceanogr.* 34:1510–1523.

Smith, R. C., and Baker, K. S. (1981), Optical properties of the clearest natural waters (200-800 nm), *Appl. Opt.* 20: 177–184.

Smith, R. C., and Baker, K. S. (1984), The analysis of ocean optical data, in *Ocean Optics VII*, Proc. SPIE 489, pp. 119–126.

Smith, R. C., and Baker, K. S. (1986), The analysis of ocean optical data, 2, in *Ocean Optics VIII*, Proc. SPIE 637, pp. 95–107.

Stavn, R. H. (1990), Raman scattering effects at the shorter visible wavelengths in clear ocean waters, in *Ocean Optics X*, Proc. SPIE 1302, pp. 94–100.

Vane, G., Green, R. O., Chrien, T. G., Enmark, H. T., Hansen, E. G., and Porter, W. M. (1993), The airborne visible / infrared imaging spectrometer (AVIRIS), *Remote Sens. Environ.* 44:127–143.